# An optical tweezer array of ultracold polyatomic molecules

https://doi.org/10.1038/s41586-024-07199-1

Received: 15 November 2023

Accepted: 13 February 2024

Published online: 3 April 2024



Check for updates

Nathaniel B. Vilas<sup>1,2™</sup>, Paige Robichaud<sup>1,2</sup>, Christian Hallas<sup>1,2</sup>, Grace K. Li<sup>1,2</sup>, Loïc Anderegg<sup>1,2</sup> & John M. Dovle<sup>1,2</sup>

Polyatomic molecules have rich structural features that make them uniquely suited to applications in quantum information science<sup>1-3</sup>, quantum simulation<sup>4-6</sup>, ultracold chemistry<sup>7</sup> and searches for physics beyond the standard model<sup>8-10</sup>. However, a key challenge is fully controlling both the internal quantum state and the motional degrees of freedom of the molecules. Here we demonstrate the creation of an optical tweezer array of individual polyatomic molecules, CaOH, with quantum control of their internal quantum state. The complex quantum structure of CaOH results in a non-trivial dependence of the molecules' behaviour on the tweezer light wavelength. We control this interaction and directly and non-destructively image individual molecules in the tweezer array with a fidelity greater than 90%. The molecules are manipulated at the single internal quantum state level, thus demonstrating coherent state control in a tweezer array. The platform demonstrated here will enable a variety of experiments using individual polyatomic molecules with arbitrary spatial arrangement.

Ultracold molecules are an important frontier in quantum science due to their rich internal structure and large intrinsic electric dipole moments, and as a bridge between ultracold physics and quantum chemistry. Identified scientific applications include quantum simulation<sup>5,11,12</sup>, quantum information processing<sup>1-3,13-17</sup>, quantum chemistry<sup>7</sup>, collisional physics<sup>18</sup>, quantum metrology and clocks<sup>19</sup>, and precision searches for physics beyond the standard model<sup>8,9,20</sup>. One promising platform for realizing many of these goals is an optical tweezer array, which can allow for positioning of individually trapped particles in arbitrary geometries, as well as dynamic rearrangement of their positions<sup>21-23</sup>. Optical tweezer arrays have already proven to be extremely successful for ultracold atoms<sup>24,25</sup>, enabling the realization of high-fidelity quantum processors<sup>23,26,27</sup> and quantum simulators<sup>28-30</sup> based on Rydberg interactions, as well as the development of  $tweezer-based\ optical\ clocks\ for\ precision\ metrology^{31-33}\ and\ the\ study$ of ultracold collisions<sup>34</sup>. Tweezer arrays of diatomic molecules have also been achieved<sup>35–37</sup>, as has the observation of dipolar interactions and two-molecule entangling gates<sup>38,39</sup>. Recently, Raman sideband cooling of these molecules to the motional ground state of the trap has demonstrated full quantum control of both internal and external states of laser-cooled diatomic molecules 40,41.

Polyatomic molecules, as compared to atoms and diatomic molecules, have non-trivial additional degrees of freedom that can be harnessed for quantum science and technology and precision measurement applications<sup>42</sup>. For example, polyatomic molecules generically contain very closely spaced opposite-parity states that allow the molecule to be polarized in the laboratory frame using small applied electric fields, with a structure that is ideal for many applications  $^{1.8,10}$ . Such states allow quantum information processing schemes with switchable dipole-dipole interactions<sup>1,2</sup>, as well as natural simulation of quantum magnetism models<sup>4-6</sup>. The large number of internal states in polyatomic molecules could also be useful for encoding error-corrected qubit states 17, or for creating qudit 16 states enabling many bits of quantum information to be contained in a single physical molecule. Additionally, polyatomic molecules are promising for searches for physics beyond the standard model, as they contain states with high beyond-the-standard-model sensitivity and strong isolation from background noise and decoherence sources<sup>8,9,43,44</sup>. All of these applications could either be enabled by, or benefit from, isolating and controlling individual polyatomic molecules in optical tweezer arrays. Towards these scientific goals, polyatomic molecules have been laser cooled 42,45,46 and trapped in electrostatic 47,48, magnetic 49 and optical<sup>43,50</sup> traps, but they have not previously been controlled at the single-particle level.

In this work, we demonstrate trapping of polyatomic molecules in an array of optical tweezers. Laser-cooled CaOH molecules are trapped in a magneto-optical trap (MOT) and transferred into a large optical dipole trap (ODT), and then single molecules are loaded into optical tweezers. During loading, a collisional blockade occurs<sup>51</sup>, ensuring that each tweezer contains at most one molecule. The molecules are non-destructively imaged in the tweezers, enabling identification of loaded tweezers and re-imaging later in the experimental sequence. We observe that the loading and imaging efficiencies depend strongly on the tweezer light wavelength due to the rich spectrum of excited states in CaOH. We characterize this dependence and determine optimal parameters to control these effects. Finally, we prepare individually trapped CaOH molecules in a single quantum state within the lowest-lying parity-doubled vibrational bending mode, an identified resource for many quantum science goals.

#### **Experimental overview**

The experiment begins with approximately 10<sup>4</sup> laser-cooled CaOH molecules loaded in a magneto-optical trap (MOT) at approximately

Department of Physics, Harvard University, Cambridge, MA, USA, <sup>2</sup>Harvard-MIT Center for Ultracold Atoms, Cambridge, MA, USA, <sup>™</sup>e-mail; vilas@g,harvard.edu

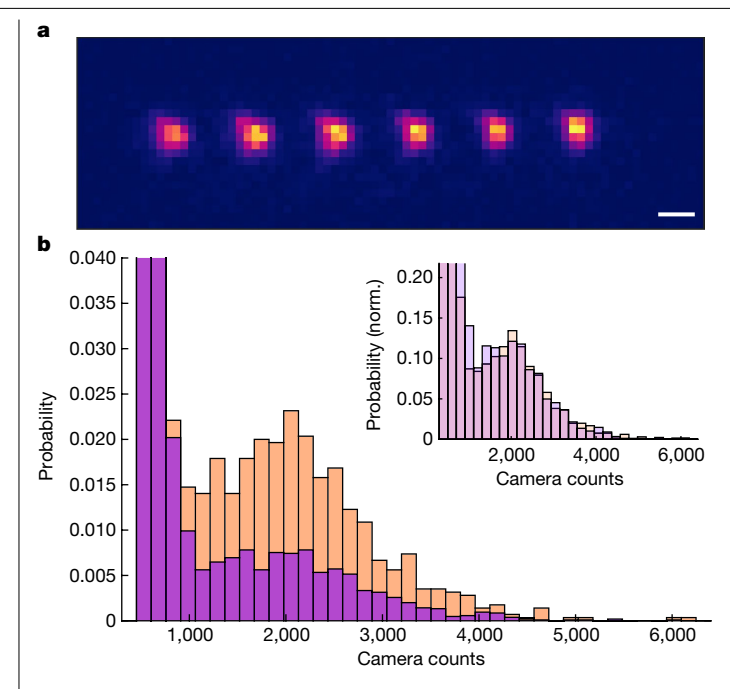


Fig. 1 | An optical tweezer array of CaOH molecules. a. Averaged image of the CaOH tweezer array, attained by imaging the molecules for a 50 ms duration and averaging over hundreds of iterations of the experimental sequence. Scale bar,  $5 \, \mu m \, b$ , Histograms of collected fluorescence for  $15 \, ms$  duration tweezer images at average loading probabilities of 31% (orange) and 13% (purple). Inset, histograms normalized (norm.) by loading rate, indicating that the shape of the loaded molecule peak does not change with the loading probability.

1 mK (ref. 46). The molecules are next cooled into an ODT<sup>50</sup>, and then into six optical tweezer traps projected inside the ODT (Methods). After loading, a final cooling pulse is applied to induce light-assisted collisions in multiply occupied tweezers, leaving at most a single molecule remaining in each trap<sup>51</sup>.

Molecules in the tweezers are imaged using  $\Lambda$ -enhanced grey molasses cooling, which allows thousands of photons to be scattered 50,52. Fluorescence from the  $\widetilde{A}^2\Pi_{1/2}(000) \rightarrow \widetilde{X}^2\Sigma^+(000)$  cooling transition at 626 nm is collected via the lens used to project the tweezers, and then imaged onto an electron multiplying charge-coupled device (EMCCD) camera. We find that optimal imaging occurs only at specific tweezer wavelengths and requires several of the vibrational repumping lasers used for imaging to be tuned by approximately 100 MHz from their free-space values, as discussed in detail below. Figure 1a shows an averaged image of the tweezer array.

Histogram analysis of the intensity of fluorescence from the molecules reveals single-molecule trapping in the tweezers. Figure 1b shows histograms of camera counts attained from fluorescence imaging of the molecules in tweezers. Histograms are shown for 15 ms images and for two average tweezer loading probabilities of 31% (orange) and 13% (purple), tuned by varying the number of molecules loaded in the MOT. The narrow peak on the left corresponds to empty tweezers, while the broader peak on the right corresponds to loaded tweezers; choosing a threshold value between the two peaks enables classification of single shot images as corresponding to loaded or empty tweezers. As shown in the inset of Fig. 1b, rescaling the histograms by their respective loading rates shows that they have identical shapes. This is only possible if single molecules are loaded; otherwise, reducing the loading rate would lower the average number of molecules loaded, and thereby decrease the average brightness while altering the qualitative shape of the histograms. From quantitative analysis of the histograms, we identify the residual fraction of loaded traps containing more than one molecule to be  $5 \pm 5\%$  (Methods).

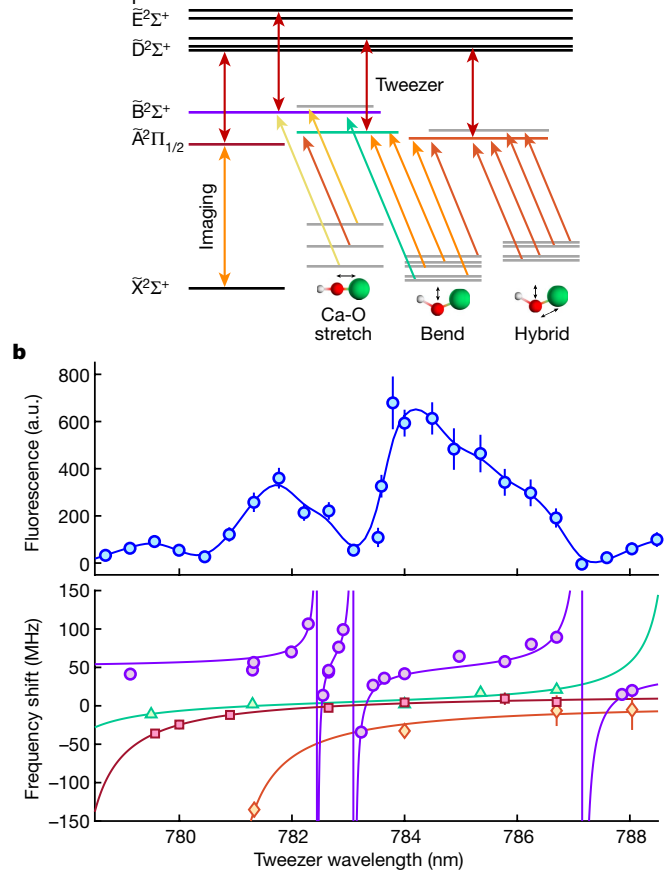


Fig. 2 | Wavelength dependence of CaOH trapping. a, Level diagram showing the cooling and repumping lasers used for  $\Lambda$  imaging (arrows connecting  $\tilde{X}^{T}\Sigma^{+}$  to the  $\widetilde{A}^2\Pi_{1/2}$  and  $\widetilde{B}^2\Sigma^+$  manifolds), as well as the high-lying electronic states to which the approximately 780 nm tweezer light (dark red arrows) couples. **b**, Top plot, average tweezer fluorescence versus wavelength for 50 ms array images. The solid curve is a guide to the eye. Bottom plot, measured relative a.c. Stark shifts of the  $\widetilde{A}^2\Pi_{1/2}(000)$  (red squares),  $\widetilde{B}^2\Sigma^+(000)$  (purple circles),  $\widetilde{A}^2\Pi_{1/2}(100)$  (green triangles) and  $\widetilde{A}(010)\kappa^2\Sigma^{(-)}$  (orange diamonds) states. Solid curves are fits used to extract line positions and coupling strengths (Methods). Error bars represent 68% confidence intervals.

#### **Excited electronic states**

A general challenge of optically manipulating and trapping polyatomic molecules is the relatively large density of excited states compared to atoms and diatomic molecules. This shows up specifically in our experiment as molecular loss dependent on the wavelength of the tweezer light. We characterize the manifold of excited states near the tweezer wavelength, model the interactions of the molecules with the tweezer light and are then able to tune the wavelength of the tweezer light to control loss.

Energy levels relevant to molecular imaging are shown in Fig. 2a. The high-lying electronic potentials  $\widetilde{D}^2\Sigma^+$ ,  $\widetilde{E}^2\Sigma^+$  and  $\widetilde{F}$  (ref. 53) are coupled to the  $\widetilde{A}^2\Pi_{1/2}$  and  $\widetilde{B}^2\Sigma^+$  states by the tweezer light. This has the effect of (1) shifting cooling and repumping imaging lasers out of resonance due to a.c. Stark shifts and (2) sometimes directly exciting molecules to these electronic states, which can lead to loss from imaging excitation.

Figure 2b (top plot) plots the overall brightness of molecules in the tweezers (a combination of loading fraction and imaging efficiency) as a function of tweezer light wavelength over the range 779-788 nm. This was done using fixed imaging and repumping frequencies chosen to optimize the signal at 784 nm. While bright tweezers are observable

around 784 nm and 782 nm, they are very dim in several wavelength regions, notably around 783 nm, above 787 nm and below 780 nm.

To characterize the wavelength dependence, we measure the a.c. Stark shifts of the laser cooling excited states as a function of tweezer wavelength (Fig. 2b, bottom plot). Specifically, we study the  $\widetilde{A}(000)$ ,  $\widetilde{B}(000)$ ,  $\widetilde{A}(100)$  and  $\widetilde{A}(010)$  states, which are the most important excited states used for CaOH optical cycling  $^{46}$ . At each tweezer wavelength, we scan the frequency of a cooling or repumping laser addressing the target electronic state in order to maximize the tweezer brightness during imaging (Methods). The offset between the optimal frequency and the known free-space resonance is the a.c. Stark shift.

We fit the observed Stark shifts to analytic lineshapes to determine the position and strength of the excited-state couplings (Methods). The energy of the  $\widetilde{A}(000)$  excited state exhibits a resonance at 777.9(6) nm, which is consistent with the expected wavelength for coupling from  $\widetilde{A}^2\Pi_{1/2}(000) \to \widetilde{D}^2\Sigma^+(100)$  (ref. 53). The other  $\widetilde{A}^2\Pi_{1/2}$  state vibrational levels exhibit similar behaviour, due to coupling with vibrational levels of the  $\widetilde{D}^2\Sigma^+$  electronic potential.

While the resonances observed in the  $\widetilde{A}^2\Pi_{1/2}$  excited states were expected based on previous state assignments in the literature  $^{53}$ , the  $\widetilde{B}^2\Sigma^\dagger(000)$  state is shifted by high-lying states with no known literature assignment. Three features are observed in our data, at 782.4(1) nm, 783.1(1) nm and 787.2(1) nm, corresponding to unassigned excited states in CaOH at 30,804(2) cm $^{-1}$ , 30,792(2) cm $^{-1}$  and 30,726(2) cm $^{-1}$ , respectively. These states lie slightly above known vibrational levels of the  $\widetilde{E}^2\Sigma^\dagger$  and  $\widetilde{F}$  electronic states  $^{53}$  and therefore likely belong to one or both of those electronic manifolds. Based on this data, we choose an optimal tweezer wavelength of 784.5 nm, which is well separated from the observed resonances and results in minimal loss.

# Imaging of molecules in the tweezers

We image CaOH molecules in the tweezer array using grey molasses cooling light in a  $\Lambda$  configuration  $^{50,52}$ , as shown in Fig. 3a. The imaging parameters are chosen to maximize the number of photons that can be scattered from each tweezer-trapped molecule, and several repumping lasers are detuned to compensate for the excited-state a.c. Stark shifts (Methods). Fluorescence histograms collected using a 15 ms imaging duration are shown in Fig. 1b.

The imaging lifetime,  $\tau$ , is the average time the molecules survive during imaging before being lost from the tweezer or falling into a molecular dark state. To measure  $\tau$  and the photon scattering rate of the molecules,  $\Gamma$ , we image for a variable duration, then wait 50 ms and image a second time (15 ms duration). The molecule survival (defined as the conditional probability that a molecule is detected in the second image, given that it was present in the first image) is plotted in Fig. 3b as a function of the first image duration. The data are fit to an exponential decay with a 1/e imaging lifetime of  $\tau = 32(3)$  ms. We also find for long imaging times  $t \gg \tau$  that each molecule scatters  $N_{\rm im} = 8(1) \times 10^3$  photons, on average, before going dark to the imaging light (Methods). Combining these measurements, we determine that the photon scattering rate is  $\Gamma = 250(40) \times 10^3$  s<sup>-1</sup> during imaging. We measure the molecule lifetime in the absence of imaging light to be 690(70) ms, which is determined predominantly by imperfect vacuum and by blackbody excitation (Fig. 3c)50,54.

The average number of photons scattered during long imaging pulses,  $N_{\rm im}$ , is slightly less than the expected limit of approximately  $1.6\times10^4$  photons from loss to known dark vibrational states (Methods)<sup>46</sup>. We attribute the additional loss primarily to scattering from the tweezer light during imaging, which we model using the excited electronic state data from above, as described in the Methods<sup>55</sup>.

We measure the temperature of the molecules in tweezers after imaging using the release–recapture method (Fig. 3d)<sup>56</sup>, described in the Methods. For optimal imaging parameters, we measure the molecule temperature to be  $T = 120(10) \mu$ K, corresponding to a ratio of trap depth

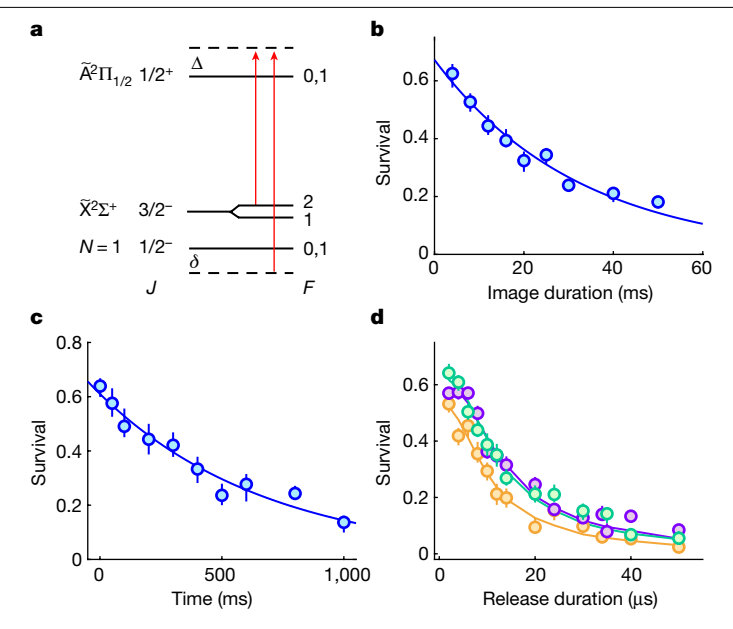


**Fig. 3** | **Tweezer array imaging and characterization. a**, Laser configuration used for  $\Lambda$  imaging of the tweezer array, where  $\Delta$  is the single-photon detuning and  $\delta$  is the two-photon detuning. **b**, Lifetime of CaOH molecules during imaging, measured to be 32(3) ms. **c**, Tweezer hold lifetime, measured to be 690(70) ms, limited predominantly by background gas and blackbody excitation  $^{50,54}$ . **d**, Release–recapture temperature measurements for single-photon detunings of  $\Delta$  = 16 MHz (orange), 22 MHz (purple) and 28 MHz (green). Solid curves show Monte Carlo fit results, indicating ratios of trap depth to temperature  $\eta$  = 6(2),12(1) and 9(1), respectively. Error bars represent 68% confidence intervals.

to molecule temperature of  $\eta$  = 12(1). Increasing the single-photon detuning by 6 MHz increases the temperature ratio to  $\eta$  = 9(1) but causes no decrease in the maximum number of photons scattered. This suggests that the imaging lifetime is not limited by the molecule temperature.

One key feature of the optical tweezer platform is the ability to image molecules non-destructively, for example in order to postselect data on loaded tweezers or to rearrange the molecules into ordered arrays  $^{21}$ . Doing so requires the ability to distinguish loaded from empty tweezers with high fidelity while minimizing molecule loss. We find that an imaging duration of 7 ms achieves a satisfactory balance between these requirements. Using a background subtraction procedure described in the Methods, we determine that the imaging fidelity after 7 ms of imaging is  $0.94^{+0.02}_{-0.03}$  for a tweezer loading rate of 34%, while the probability of the molecule surviving after the image is 80%. Higher molecule survival probabilities can be attained by imaging for even shorter durations, at the cost of more frequently misidentifying loaded traps as empty. The detection fidelity is limited by the finite molecule imaging lifetime in combination with our photon collection efficiency, and does not increase significantly for longer imaging durations.

# Single quantum state preparation and control

Next, we demonstrate coherent control of the internal states of CaOH molecules in the optical tweezer array. We begin by optically transferring molecular population into the  $\widetilde{X}^2\Sigma^+(010)$  vibrational bending mode, whose  $\ell$ -type parity-doublet structure is useful for many quantum science applications<sup>1,6,8,43,57</sup>. Unlike in our previous work with CaOH in an ODT, where approximately 1,200 photons were scattered during this step<sup>50</sup>, here with tweezers we optically pump using only approximately 2 photons by exciting the  $\widetilde{X}^2\Sigma^+(000)(N=1^-) \to \widetilde{A}^2\Pi(010)\kappa^2\Sigma^{(-)}(J=1/2^+)$  transition at 609 nm. The excited state decays

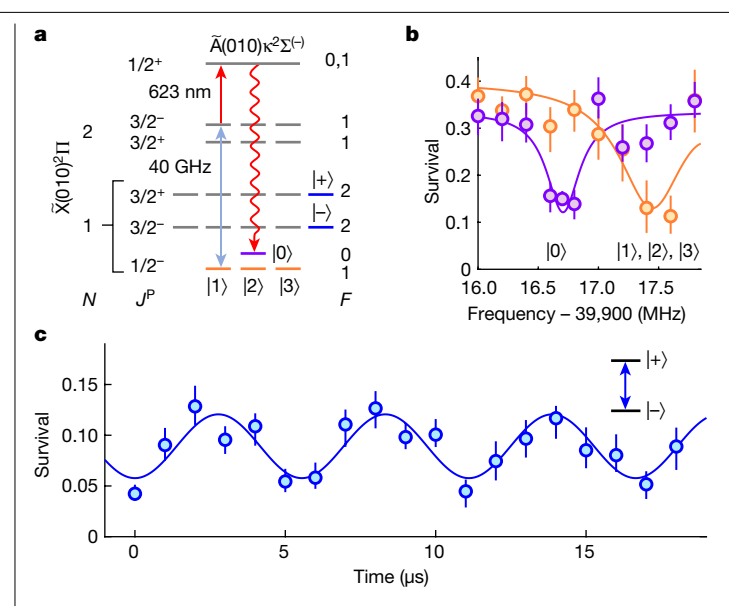


Fig. 4 | Single-state control of CaOH in optical tweezers. a, Microwaveoptical scheme for pumping population into the single quantum state  $|0\rangle$  $(F = 0^{-})$  in the  $\tilde{X}(010)$  bending mode. Microwave radiation at 40 GHz resolves  $|0\rangle$ from the nearby states  $|1\rangle$ ,  $|2\rangle$  and  $|3\rangle$ , while a 623 nm laser dissipatively returns population to states |0\rangle through |3\rangle. Also shown are the parity-doublet states  $|+\rangle$   $(F=2^+, m_F=2)$  and  $|-\rangle$   $(F=2^-, m_F=2)$ . Nearby hyperfine levels are omitted from the figure for clarity. **b**, Depletion spectroscopy of the  $N=1, J=1/2^- \rightarrow N=2$ ,  $J = 3/2^+$  microwave transitions before (orange) and after (purple) optical pumping, demonstrating accumulation of population in |0 \( (leftmost peak). **c**, Rabi oscillations on the  $|-\rangle \leftrightarrow |+\rangle$  parity-doublet transition at 43 MHz. Error bars represent 68% confidence intervals.

to the N = 1,  $J = 1/2^-$  and N = 2,  $J = 3/2^-$  states in the bending mode with approximately equal probability, and the N = 2,  $J = 3/2^-$  population is repumped back through  $\tilde{A}(010)$  and into N=1. After optical transfer, the tweezer trap depth is reduced by 80% in preparation for further state manipulation.

After transfer into the vibrational bending mode, population is predominantly contained in the four hyperfine sublevels of the N=1,  $J=1/2^$ manifold, which we label  $|0\rangle$ ,  $|1\rangle$ ,  $|2\rangle$  and  $|3\rangle$  (Fig. 4a). We optically pump the majority of this population into  $|0\rangle \equiv (F=0, m_E=0)$  using the microwave-optical pumping scheme outlined in Fig. 4a, as demonstrated in previous work with CaOH molecules in an ODT<sup>43</sup>. A microwave field at approximately 40 GHz resonantly couples states  $|1\rangle$ ,  $|2\rangle$  and  $|3\rangle$  to N=2,  $J=3/2^-$  in the presence of a small electric field (7.5 V cm<sup>-1</sup>), while state  $|0\rangle$  is sufficiently detuned (by approximately 1.4 MHz) to remain dark to the microwaves. A 623 nm laser drives the N = 2,  $J = 3/2^$ population to  $\widetilde{A}(010)\kappa^2\Sigma^{(-)}(I=1/2^+)$ , which spontaneously decays to  $|0\rangle$ ... $|3\rangle$  with approximately 55% probability, and back to  $N=2, J=3/2^$ otherwise (with a small approximately 1% fraction lost to unaddressed levels). Population therefore accumulates in  $|0\rangle$  after approximately 7 photons are scattered. Finally, we perform microwave spectroscopy to read out the hyperfine state populations (Methods). As shown in Fig. 4b, we find that the molecular population is predominantly contained in the near-degenerate  $F = 1^-$  states ( $|1\rangle$ ,  $|2\rangle$  and  $|3\rangle$ ) in the absence of optical pumping (orange data), while a majority of the molecular population is transferred into |0\range after optical pumping is applied (purple data).

After optical pumping, we demonstrate coherent control of CaOH molecules in the optical tweezer array by driving Rabi oscillations on a parity-doublet transition in the bending mode. We choose the hyperfine stretched states  $|+\rangle \equiv (F=2^+, m_F=2)$  and  $|-\rangle \equiv (F=2^-, m_F=2)$  due to their large transition dipole moment, which would enable strong dipolar spin-exchange interactions between adjacent molecules and

make them promising qubit states. We begin by transferring population from  $|0\rangle$  to  $|+\rangle$  with a radio-frequency  $\pi$  pulse in the presence of a small magnetic field B = 2 G. We then resonantly drive the  $|+\rangle \leftrightarrow |-\rangle$ parity-doublet transition with a 43 MHz radio-frequency field. The population detected in  $|-\rangle$  as a function of drive time is shown in Fig. 4c, demonstrating clear Rabi oscillations with a frequency  $\Omega = 2\pi \times 180$  kHz.

#### **Summary and outlook**

In summary, we have realized an array of single CaOH molecules by directly loading laser-cooled molecules into tightly focused optical tweezer traps at 785 nm. We directly and non-destructively image individual trapped molecules and achieve fidelities greater than 90% for distinguishing loaded from empty traps. We have characterized the trap-wavelength dependence of the tweezer imaging, which is found to be limited by tweezer light-mediated coupling to high-lying electronic states in CaOH. Finally, we prepared CaOH molecules in the tweezer array in single quantum states and observed coherent Rabi oscillations on a parity-doublet transition in the vibrational bending mode.

These results pave the way for numerous experiments in quantum information science<sup>1,2</sup>, quantum simulation<sup>4,6</sup>, ultracold collisions<sup>18,57,58</sup> and precision measurements<sup>8,9,43</sup> that require (or could benefit from) the combination of full internal and external state control of individual polyatomic molecules, as provided by the optical tweezer platform. The platform demonstrated here can be used in the near term to realize dipolar interactions between molecules in adjacent optical tweezers in parity-doublet states and for cooling of the molecules' motion to the quantum regime<sup>40,41</sup>. The imaging fidelities achieved here could be increased in future work by using longer tweezer light wavelengths, for example, 1,064 nm, which we successfully used to optically trap CaOH in larger optical dipole traps<sup>50</sup>. Finally, this work is expected to be extendable to larger and/or more complex polyatomic molecules amenable to direct laser cooling techniques, including symmetric and asymmetric top molecules<sup>59,60</sup>.

# **Online content**

Any methods, additional references, Nature Portfolio reporting summaries, source data, extended data, supplementary information, acknowledgements, peer review information; details of author contributions and competing interests; and statements of data and code availability are available at https://doi.org/10.1038/s41586-024-07199-1.

- Yu, P., Cheuk, L. W., Kozyryev, I. & Doyle, J. M. A scalable quantum computing platform using symmetric-top molecules. New J. Phys. 21, 093049 (2019).
- Wei, Q., Kais, S., Friedrich, B. & Herschbach, D. Entanglement of polar symmetric top molecules as candidate qubits. J. Chem. Phys. 135, 154102 (2011).
- Tesch, C. M. & de Vivie-Riedle, R. Quantum computation with vibrationally excited molecules, Phys. Rev. Lett. 89, 157901 (2002).
- Wall, M. L., Maeda, K. & Carr, L. D. Simulating quantum magnets with symmetric top molecules, Ann. Phys. (Berlin) 525, 845-865 (2013).
- Wall, M., Hazzard, K. & Rev, A. M. in From Atomic To Mesoscale: The Role of Quantum Coherence in Systems of Various Complexities (eds Malinovskaya, S. & Novikoya, I.) 3-37 (World Scientific, 2015).
- Wall, M., Maeda, K. & Carr, L. D. Realizing unconventional quantum magnetism with symmetric top molecules. New J. Phys. 17, 025001 (2015).
- Heazlewood, B. R. & Softley, T. P. Towards chemistry at absolute zero. Nat. Rev. Chem. 5, 125-140 (2021).
- Kozyryev, I. & Hutzler, N. R. Precision measurement of time-reversal symmetry violation with laser-cooled polyatomic molecules. Phys. Rev. Lett. 119, 133002 (2017).
- Kozyryev, I., Lasner, Z. & Doyle, J. M. Enhanced sensitivity to ultralight bosonic dark matter in the spectra of the linear radical SrOH. Phys. Rev. A 103, 043313 (2021)
- 10. Hutzler, N. R. Polyatomic molecules as quantum sensors for fundamental physics. Quantum Sci. Technol. 5, 044011 (2020).
- Micheli, A., Brennen, G. & Zoller, P. A toolbox for lattice-spin models with polar molecules. Nat. Phys. 2, 341-347 (2006)
- Gorshkov, A. V. et al. Quantum magnetism with polar alkali-metal dimers. Phys. Rev. A 84,
- DeMille, D. Quantum computation with trapped polar molecules. Phys. Rev. Lett. 88,
- Yelin, S., Kirby, K. & Côté, R. Schemes for robust quantum computation with polar molecules. Phys. Rev. A 74, 050301 (2006).

- Ni, K.-K., Rosenband, T. & Grimes, D. D. Dipolar exchange quantum logic gate with polar molecules. Chem. Sci. 9, 6830–6838 (2018).
- 16. Sawant, R. et al. Ultracold polar molecules as qudits. *New J. Phys.* **22**, 013027 (2020).
- Albert, V. V., Covey, J. P. & Preskill, J. Robust encoding of a qubit in a molecule. Phys. Rev. X 10, 031050 (2020).
- Cheuk, L. W. et al. Observation of collisions between two ultracold ground-state Caf molecules. Phys. Rev. Lett. 125, 043401 (2020).
- Kondov, S. S. et al. Molecular lattice clock with long vibrational coherence. Nat. Phys. 15, 1118–1122 (2019).
- Norrgard, E. B. et al. Nuclear-spin dependent parity violation in optically trapped polyatomic molecules. Commun. Phys. 2, 1–6 (2019).
- Endres, M. et al. Atom-by-atom assembly of defect-free one-dimensional cold atom arrays. Science 354, 1024–1027 (2016).
- Barredo, D., Lienhard, V., de Léséleuc, S., Lahaye, T. & Browaeys, A. Synthetic threedimensional atomic structures assembled atom by atom. *Nature* 561, 79–82 (2018).
- Bluvstein, D. et al. A quantum processor based on coherent transport of entangled atom arrays. Nature 604, 451–456 (2022).
- Kaufman, A. M. & Ni, K.-K. Quantum science with optical tweezer arrays of ultracold atoms and molecules. Nat. Phys. 17, 1324–1333 (2021).
- Browaeys, A. & Lahaye, T. Many-body physics with individually controlled Rydberg atoms. Nat. Phys. 16, 132–142 (2020).
- Levine, H. et al. Parallel implementation of high-fidelity multiqubit gates with neutral atoms. Phys. Rev. Lett. 123, 170503 (2019).
- Evered, S. J. et al. High-fidelity parallel entangling gates on a neutral-atom quantum computer. Nature 622, 268–272 (2023).
- Bernien, H. et al. Probing many-body dynamics on a 51-atom quantum simulator. Nature 551, 579–584 (2017).
- Ebadi, S. et al. Quantum phases of matter on a 256-atom programmable quantum simulator. Nature 595, 227–232 (2021).
- Scholl, P. et al. Quantum simulation of 2D antiferromagnets with hundreds of Rydberg atoms. Nature 595, 233–238 (2021).
- Norcia, M. A. et al. Seconds-scale coherence on an optical clock transition in a tweezer array. Science 366, 93–97 (2019).
- 32. Madjarov, I. S. et al. An atomic-array optical clock with single-atom readout. *Phys. Rev. X* **9**, 041052 (2019).
- Young, A. W. et al. Half-minute-scale atomic coherence and high relative stability in a tweezer clock. Nature 588, 408–413 (2020).
- Reynolds, L. A. et al. Direct measurements of collisional dynamics in cold atom triads. *Phys. Rev. Lett.* 124, 073401 (2020).
- Anderegg, L. et al. An optical tweezer array of ultracold molecules. Science 365, 1156–1158 (2019).
- Zhang, J. T. et al. An optical tweezer array of ground-state polar molecules. Quantum Sci. Technol. 7, 035006 (2022).
- Ruttley, D. K. et al. Formation of ultracold molecules by merging optical tweezers. Phys. Rev. Lett. 130, 223401 (2023).
- 38. Holland, C. M., Lu, Y. & Cheuk, L. W. On-demand entanglement of molecules in a reconfigurable optical tweezer array. *Science* **382**, 1143–1147 (2023).
- Bao, Y. et al. Dipolar spin-exchange and entanglement between molecules in an optical tweezer array. Science 382, 1138–1143 (2023).
- Bao, Y. et al. Raman sideband cooling of molecules in an optical tweezer array to the 3D motional ground state. Preprint at https://arxiv.org/abs/2309.08706 (2023).

- 41. Lu, Y., Li, S. J., Holland, C. M. & Cheuk, L. W. Raman sideband cooling of molecules in an optical tweezer array. *Nat. Phys.* **20**, 389–394 (2024).
- 42. Augenbraun, B. L. et al. in Advances in Atomic, Molecular, and Optical Physics Vol. 72 (eds DiMauro, L. F., Perrin, H. & Yelin, S. F.) 89–182 (Academic, 2023).
- Anderegg, L. et al. Quantum control of trapped polyatomic molecules for eEDM searches. Science 382, 665–668 (2023).
- Takahashi, Y., Zhang, C., Jadbabaie, A. & Hutzler, N. R. Engineering field-insensitive molecular clock transitions for symmetry violation searches. *Phys. Rev. Lett.* 131, 183003 (2023).
- Kozyryev, I. et al. Sisyphus laser cooling of a polyatomic molecule. Phys. Rev. Lett. 118, 173201 (2017).
- Vilas, N. B. et al. Magneto-optical trapping and sub-Doppler cooling of a polyatomic molecule. Nature 606, 70-74 (2022).
- Zeppenfeld, M. et al. Sisyphus cooling of electrically trapped polyatomic molecules. Nature 491, 570 (2012).
- 48. Prehn, A., Ibrügger, M., Glöckner, R., Rempe, G. & Zeppenfeld, M. Optoelectrical cooling of polar molecules to submillikelvin temperatures. *Phys. Rev. Lett.* **116**, 063005 (2016).
- 49. Liu, Y. et al. Magnetic trapping of cold methyl radicals. *Phys. Rev. Lett.* **118**, 093201 (2017).
- Hallas, C. et al. Optical trapping of a polyatomic molecule in an ℓ-type parity doublet state. Phys. Rev. Lett. 130, 153202 (2023).
- 51. Schlosser, N., Reymond, G., Protsenko, I. & Grangier, P. Sub-poissonian loading of single atoms in a microscopic dipole trap. *Nature* **411**, 1024–1027 (2001).
- Cheuk, L. W. et al. A-enhanced imaging of molecules in an optical trap. Phys. Rev. Lett. 121, 083201 (2018).
- Pereira, R. & Levy, D. H. Observation and spectroscopy of high-lying states of the CaOH radical: Evidence for a bent, covalent state. J. Chem. Phys. 105, 9733–9739 (1996).
- Vilas, N. B. et al. Blackbody thermalization and vibrational lifetimes of trapped polyatomic molecules. *Phys. Rev. A* 107, 062802 (2023).
- Holland, C. M., Lu, Y. & Cheuk, L. W. Bichromatic imaging of single molecules in an optical tweezer array. Phys. Rev. Lett. 131, 053202 (2023).
- Tuchendler, C., Lance, A. M., Browaeys, A., Sortais, Y. R. P. & Grangier, P. Energy distribution and cooling of a single atom in an optical tweezer. *Phys. Rev. A* 78, 033425 (2008)
- Augustovičová, L. D. & Bohn, J. L. Ultracold collisions of polyatomic molecules: CaOH. New J. Phys. 21, 103022 (2019).
- Anderegg, L. et al. Observation of microwave shielding of ultracold molecules. Science 373, 779–782 (2021).
- Mitra, D. et al. Direct laser cooling of a symmetric top molecule. Science 369, 1366–1369 (2020).
- Augenbraun, B. L., Doyle, J. M., Zelevinsky, T. & Kozyryev, I. Molecular asymmetry and optical cycling: Laser cooling asymmetric top molecules. *Phys. Rev. X* 10, 031022 (2020).

**Publisher's note** Springer Nature remains neutral with regard to jurisdictional claims in published maps and institutional affiliations.

Springer Nature or its licensor (e.g. a society or other partner) holds exclusive rights to this article under a publishing agreement with the author(s) or other rightsholder(s); author self-archiving of the accepted manuscript version of this article is solely governed by the terms of such publishing agreement and applicable law.

© The Author(s), under exclusive licence to Springer Nature Limited 2024

# **Methods**

#### State labelling notation

The notation used for labelling the molecular states is as follows.  $\widetilde{X}^2\Sigma^+$ ,  $\widetilde{A}^2\Pi$  and so on are electronic states, sometimes abbreviated as  $\widetilde{X}$ ,  $\widetilde{A}$  and so on. The vibrational state notation is  $(v_1v_2'v_3)$ , where  $v_1$  is the vibrational quantum number for the symmetric (Ca–O) stretch vibration,  $v_2$  for the Ca–O–H bending vibration and  $v_3$  for the antisymmetric (O–H) stretch vibration. The vibrational angular momentum quantum number,  $\ell \in \{v_2, v_2 - 2, ..., -v_2\}$ , is omitted for simplicity unless  $v_2 > 1$ . The angular momentum quantum numbers used are as follows. F is the total angular momentum,  $m_F$  is its projection onto the laboratory quantization axis, J is the total angular momentum excluding nuclear spin and N is the angular momentum excluding both nuclear and electron spin. A (±) superscript refers to the total parity of the state.

#### **Experimental details**

The beginning of our experimental sequence is similar to that used in previous work  $^{43,46,50}$ , with small modifications. CaOH molecules are produced in a cryogenic buffer-gas beam, radiatively slowed using the frequency-chirped slowing method  $^{61,62}$  and trapped in a magneto-optical trap (MOT)  $^{46}$ . The vibrational repumping scheme is the same as described in ref. 46, except that an additional repumping laser addressing the  $\widetilde{X}^2\Sigma^+(03^10)(N''=1)\to\widetilde{A}(010)\mu^2\Sigma^{(+)}(J'=1/2^+)$  transition at 655 nm has been added. This increases the vibrational-decay-limited average number of photons scattered per molecule from approximately 12,000 to approximately 16,000.

The optical dipole trap (ODT) and optical tweezers are loaded using a 5 ms Λ-enhanced grey molasses cooling pulse followed by 80 ms of single-frequency cooling<sup>50</sup>. The ODT is necessary to achieve sufficient density for efficient tweezer loading<sup>35</sup>, and the ODT and tweezers remain on for the full cooling duration. The approximately 600 µK deep ODT is generated from a 13.3 W, 1,064 nm laser beam focused down to an approximately 25 µm waist in the centre of the molecular MOT<sup>50</sup>. During loading, we raster the ODT position along the tweezer array axis at a frequency of 100 Hz using a piezo-actuated mirror mount in the 1,064 nm beam path. The tweezer trap array is generated by a 784.5 nm laser beam which is diffracted by an acousto-optic deflector (AA Opto Electronic DTSX-400-780) in the Fourier plane of the imaging system to generate the individual traps. The acousto-optic deflector is driven with the sum of six radio-frequency tones centred near 100 MHz and spaced by 1.875 MHz. The relative phases of the radio-frequency tones are chosen using a random sampling procedure to minimize the peak amplitude of the summed waveform. The resulting beams are expanded and then focused through an in-vacuum aspheric lens (Edmund Optics, 25 mm diameter, 0.40 NA) to generate an array of six tweezer traps with approximately 2 µm waists, separated by 11 µm. The tweezer light is co-linear with but counterpropagating to the ODT beam.

The tweezer trap depth during loading is 1.6 mK, corresponding to approximately 150 mW of optical power per trap. After loading, a 4 ms pulse of  $\Lambda$ -imaging light  $^{50.52}$  is applied to induce light-assisted collisions in tweezers with more than one molecule loaded, ensuring a collisional blockade, wherein each tweezer contains at most one single molecule  $^{51}$ . Finally, the trap depth is reduced to 1.4 mK, which optimizes the imaging fidelity and is used for all data in Figs. 1–3.

#### Tweezer imaging

In order to minimize background scattered light during imaging of the tweezer array, six small 1.5 mm  $1/e^2$  diameter beams are used for the  $\Lambda$  imaging. These are installed at a small angle to the large 10 mm  $1/e^2$  diameter beams used for the MOT and ODT/tweezer loading, which are turned off during tweezer array imaging. Additionally, the repumping laser beam size is reduced to approximately 5 mm in diameter after radiative slowing, MOT and ODT/tweezer loading by closing

a mechanical shutter with a small aperture drilled in the centre. This is necessary because several of the repumping laser wavelengths are less than 5 nm away from the 626 nm tweezer fluorescence and are inefficiently filtered from the imaging system.

The optimal parameters for tweezer imaging are as follows (detunings are referenced relative to free-space resonance). The single-photon detuning is  $\Delta = 22$  MHz, the two-photon detuning is  $\delta = 1.25$  MHz, the sideband intensity ratio is  $I_{1/2}/I_{3/2} \approx 2$  and the total intensity is approximately 9 mW cm<sup>-2</sup> per beam. The tweezer trap depth used for imaging is 1.4 mK. Additionally, four of the repumping laser frequencies are tuned from the free-space optimal used for radiative slowing, the MOT and tweezer loading, to a.c. Stark-shifted frequencies optimized for tweezer imaging brightness. Specifically, the  $\widetilde{X}^2\Sigma^+(100) \rightarrow \widetilde{B}^2\Sigma^+(000)$ repumping laser is tuned approximately 60 MHz to the blue; the  $\widetilde{X}^2 \Sigma^+(010)(N=1) \rightarrow \widetilde{B}^2 \Sigma^+(000)$  repumping laser is tuned approximately 140 MHz to the blue; the  $\widetilde{X}^2\Sigma^+(02^00) \rightarrow \widetilde{A}^2\Pi_{1/2}(100)$  repumping laser is tuned approximately 40 MHz to the red; and the  $\widetilde{X}^2 \Sigma^+(010)(N=2) \rightarrow \widetilde{A}(010) \kappa^2 \Sigma^{(-)}$  repumping laser is tuned approximately 140 MHz to the blue. Note that the frequency spectrum of each repumping laser is broadened by approximately 300 MHz to the red of free-space resonance for radiative slowing<sup>46</sup>. This broadening remains on throughout the experimental sequence, therefore reducing the precision requirements for the tweezer repumping frequencies.

#### Single-state control and spectroscopy

Microwave-optical pumping of CaOH into a single quantum state is achieved using 40 GHz microwave radiation introduced via a horn antenna mounted outside the vacuum chamber. The optical pumping light comes from the  $\widetilde{X}^2\Sigma^+(010)(N=2) \rightarrow \widetilde{A}(010)\kappa^2\Sigma^{(-)}$  repumping laser. Radio-frequency fields for the coherent state manipulation and Rabi oscillations are introduced by directly driving the in-vacuum radio-frequency MOT coils with an oscillating voltage.

Spectroscopy used to determine the population in states  $|0\rangle\cdots|3\rangle$  before and after optical pumping (Fig. 4b) is performed by applying microwave radiation near the  $N=1,J=1/2^-,F=0,1\rightarrow N=2,J=3/2^+,F=1,2$  transitions around 39,917 MHz. Population excited to N=2 is depleted with a 627 nm laser addressing the  $\widetilde{X}^2\Sigma^+(010)(N=2,J=3/2^+)\rightarrow \widetilde{A}(010)\mu^2\Sigma^{(+)}(J=5/2^-)$  transition, which decays to rotational states that are dark to the tweezer imaging light. The spectroscopy data is acquired by imaging the tweezer array for 7 ms immediately after loading, then proceeding to transfer molecules into the bending mode, optically pump and then perform microwave spectroscopy. The molecules are then imaged for 15 ms. The plotted molecule survival is the fraction of molecules observed in the final image, conditioned on their presence in the first image. A similar procedure is used for the Rabi oscillation data in Fig. 4c, with the molecule survival determined using an initial 7 ms image before optical pumping and coherent control.

#### **Imaging system**

Fluorescence at 626 nm from the tweezer-trapped molecules is collected with the in-vacuum aspheric lens and imaged onto an EMCCD camera (Andor iXon Ultra 897). Spherical aberation correction plates  $(3 \times -1.00 \lambda)$ ; Edmund Optics) are used to compensate aberations arising from the chromatic focal shift between the 785 nm tweezers and the 626 nm fluorescence. The collection efficiency is expected to be approximately 1%, limited by the effective numerical aperture of the imaging optics (approximately 3% collection efficiency) and by transmission losses from the optical elements in the imaging path (approximately 40%). In practice, we find by comparing the observed histograms to simulations that the collection is slightly lower, likely due to imperfect alignment. Images are acquired by binning the fluorescence from each tweezer onto a single EMCCD pixel at the hardware level, minimizing the effect of camera readout noise. This procedure applies to all data presented in the main text except for the averaged image in Fig. 1a, which uses no binning.

#### Tweezer trap frequencies and trap depth

The oscillation frequencies of molecules in the optical tweezer array are measured using the parametric heating method. After loading the array, molecules are imaged for 7 ms to detect loaded traps. The trap intensity is then modulated at a variable frequency  $\omega_{\rm mod}$  for 5 ms, causing parametric heating loss when  $\omega_{\text{mod}} \approx 2\omega_i$ , where  $\omega_{i=x,y,z}$  are the trap frequencies. The tweezers are briefly shut off for 6 µs to allow heated molecules to escape, then the remaining molecules are imaged for 15 ms. The molecule survival exhibits loss features at  $\omega_{mod} = 2\pi \times 119(4)$  kHz and  $\omega_{\rm mod} = 2\pi \times 167(5)$  kHz, corresponding to radial trap frequencies of  $\omega_x = 2\pi \times 59(2)$  kHz and  $\omega_y = 2\pi \times 84(2)$  kHz. Using the calculated 780 nm dynamic polarizability for the ground state of CaOH ( $\alpha_0 = 324.3$  a.u.) (L. Cheng, private communication) and the known laser power per trap (approximately 125 mW), these frequencies imply a tweezer trap depth of  $U_0 = k_B \times 1.4$  mK (where  $k_B$  is the Boltzmann constant), an axial frequency of  $\omega_z \approx 2\pi \times 7$  kHz and slightly elliptical tweezer beams with waists  $w_x \approx 2.4 \, \mu \text{m}$  and  $w_y \approx 1.7 \, \mu \text{m}$ .

# Release-recapture temperature measurement

We measure the temperature of the molecules in tweezers after imaging using the release–recapture method  $^{56}$ , which we briefly describe here. After loading the tweezer array, we image the molecules for 7 ms to identify loaded tweezers. We then quickly switch off the tweezers, wait a variable time (on the order of  $10~\mu s$ ), switch the tweezers back on and then image a second time (15 ms imaging duration) to determine the fraction of molecules recaptured into the tweezers. The molecule survival probability versus release time is fit to a Monte Carlo simulation to extract the temperature. The results are plotted in Fig. 3d.

#### Calibration of number of photons scattered

The number of photons scattered during tweezer imaging is calibrated by comparing the collected fluorescence to reference images taken with a known number of photons limited by vibrational repumping. Specifically, to calibrate the maximum number of photons that can be scattered, we take 200 ms images in two configurations: (1) all repumping lasers on (fluorescence level  $S_1$ ), and (2) only the  $\widetilde{X}(100)$ ,  $\widetilde{X}(02^00)$ ,  $\widetilde{X}(200)$ ,  $\widetilde{X}(12^20)$  and  $\widetilde{X}(110)$  repumping lasers on, limiting the average number of photons scattered to 460 (fluorescence level  $S_2$ ) <sup>46,63</sup>. The total number of photons scattered before molecules are lost during tweezer imaging with all repumping lasers is therefore  $N_{\text{im}} = S_1/S_2 \times 460$ . For the optimal imaging parameters used in this work, we find  $N_{\text{im}} = 8(1) \times 10^3$ .

#### Modelling excited-state a.c. Stark shifts

The tweezer light is near-resonant with transitions from  $\widetilde{A}^2\Pi$  and  $\widetilde{B}^2\Sigma^+$  state vibrational levels used for laser cooling and repumping to vibrational levels of the high-lying  $\widetilde{D}^2\Sigma^+$ ,  $\widetilde{E}^2\Sigma^+$  and  $\widetilde{F}$  electronic states<sup>53</sup>. In the large detuning limit ( $\Delta \gg \Omega$ , where  $\Delta$  is the tweezer detuning and  $\Omega$  is the Rabi frequency), the effect of these couplings on the energy of excited state i is given by

$$\Delta E_i/\hbar \approx \sum_j \frac{\Omega_{ij}^2}{4(\omega_{ij} - \omega_L)} + \frac{\Omega_{ij}^2}{4(\omega_{ij} + \omega_L)}$$
 (1)

where  $\Omega_{ij}$  is the Rabi frequency for the transition from state i to state j,  $\omega_L$  is the laser frequency,  $\omega_{ij} = (E_j - E_i)/\hbar$  is the transition frequency,  $\hbar$  is the reduced Planck constant and the sum is over all molecular states j that can couple to state i.

If we restrict ourselves to a small range of wavelengths  $\Delta\lambda$  near the tweezer wavelength  $\lambda_0$ , we can make the approximation that only a small number of near-detuned states k are responsible for the wavelength dependence, and that the remaining states contribute an approximately constant energy offset  $\Delta E_{\rm off}/\hbar$  as long as they are far detuned compared to  $\Delta\lambda$ . Furthermore, we can make the rotating wave approximation and drop the second, counter-rotating term in equation (1). We find that

the wavelength dependence of the energy of state i in the range  $\Delta \lambda$ , which contains N near-detuned states k. is

$$\Delta E_i/\hbar \approx \sum_{k=1}^{N} \frac{\Omega_{ik}^2}{8\pi c (1/\lambda_L - 1/\lambda_{ik})} + \Delta E_{\text{off},i}/\hbar$$
 (2)

where  $\lambda_L = 2\pi c/\omega_L$  and  $\lambda_{ik} = 2\pi c(1/\omega_i - 1/\omega_k)$ . This expression is used to fit the a.c. Stark shift data in Fig. 2b, where the Rabi frequencies  $\Omega_{ik}$ , centre wavelengths  $\lambda_{ik}$  and energy offsets  $\Delta E_{\text{off},i}$  are fit as free parameters. We use this model-fitting approach due to a lack of complete spectroscopic data for the excited states.

#### Measured a.c. Stark shifts

The excited-state a.c. Stark shifts are measured by imaging molecules in the tweezer array with one of the repumping lasers replaced by a separate frequency-tuneable beam. At each tweezer wavelength, the frequency of the repumping beam is scanned near resonance, and the a.c. Stark shift is determined by comparing the repumping frequency that maximizes the image brightness with the known free-space resonance for the repumping transition. Because the tweezer is far detuned from all transitions out of the  $\widetilde{X}$  manifold, the wavelength dependence is assumed to arise from Stark shifts of the excited states only, while the ground state a.c. Stark shifts contribute a constant offset.

The specific transitions used are  $\widetilde{X}^2\Sigma^+(100) \rightarrow \widetilde{B}^2\Sigma^+(000), \widetilde{X}^2\Sigma^+(02^00) \rightarrow \widetilde{A}^2\Pi_{1/2}(100)$  and  $\widetilde{X}^2\Sigma^+(010)(N=2) \rightarrow \widetilde{A}(010)\kappa^2\Sigma^{(-)}$ . For the  $\widetilde{A}^2\Pi_{1/2}(000)$  state a.c. Stark shifts, the  $\widetilde{X}^2\Sigma^+(000) \rightarrow \widetilde{A}^2\Pi_{1/2}(000)$  cooling light was instead tuned during tweezer imaging, and the a.c. Stark shift was determined by comparing the optimal tweezer imaging detuning with the optimal free-space  $\Lambda$  imaging detuning. This approach is susceptible to common mode offsets in the measured a.c. Stark shift due to the need to compare with a free-space resonance frequency. However, relative frequencies and resonance wavelengths are insensitive to such offsets, meaning that the extracted transition wavelengths and transition strengths (Rabi frequencies) are robustly determined, in turn leading to accurate loss rate calculations.

The measured transition wavelengths determined from the fit to equation (2) (Fig. 2b) are as follows. The energy of the  $\widetilde{A}^2\Pi_{1/2}(000)$  excited state exhibits a resonance at 777.9(6) nm, which is consistent with the expected wavelength for coupling from  $\widetilde{A}^2\Pi_{1/2}(000) \rightarrow \widetilde{D}^2\Sigma^+(100)^{s3}$ .  $\widetilde{A}^2\Pi_{1/2}(100)$  contains resonances at 777 nm and 789 nm (consistent with coupling to  $\widetilde{D}^2\Sigma^+(200)$  and  $\widetilde{D}^2\Sigma^+(110)$ , respectively), while  $\widetilde{A}(010)\kappa^2\Sigma^{(-)}$  displays a strong resonance at 780.6 nm due to coupling with the  $\widetilde{D}^2\Sigma^+(110)$  state. Three features are observed in the  $\widetilde{B}^2\Sigma^+(000)$  data, at 782.4(1) nm, 783.1(1) nm and 787.2(1) nm, corresponding to high-lying features at 30,804(2) cm $^{-1}$ , 30,792(2) cm $^{-1}$  and 30,726(2) cm $^{-1}$ , respectively. These features fall slightly above the origin energy of the  $\widetilde{E}^2\Sigma^+$  and  $\widetilde{F}$  electronic potentials, in a frequency range not covered by previous spectroscopic literature $^{53}$ .

#### Modelling losses due to excited-state coupling

Losses arising from coupling of state i (in the laser cooling scheme) to a lossy excited state j occur at a rate  $R_{ij} = |c_{ij}|^2 \Gamma_j \rho_{ii}$ , where  $c_{ij}$  is the admixture of state j into i due to tweezer coupling,  $\Gamma_j$  is the decay rate of state j (assumed to be purely to non-detectable states) and  $\rho_{ii}$  is the molecular population in state i during tweezer imaging  $^{55}$ . In the large detuning limit  $\Delta_{ij} \gg \Omega_{ij}$ , the admixture is  $c_{ij} \approx \Omega_{ij}/(2\Delta_{ij})$ , where  $\Delta_{ij} = \omega_L - \omega_{ij}$ . The population of the laser cooling excited state i is approximately  $\rho_{ii} \approx \Gamma_{\text{scatt}}/\Gamma_i \times r_i$ , where  $\Gamma_{\text{scatt}} = 250 \times 10^3 \, \text{s}^{-1}$  is the photon scattering rate during imaging and  $r_i$  is the fraction of photon scattering events that originate from state i. The latter quantity is set by the vibrational state repumping scheme used in the experiment  $^{46}$ .

The total observed molecule loss rate during tweezer imaging is a combination of excited-state loss  $R_{ij}$ , vacuum loss  $R_{\rm vac}$  = 1/690 ms<sup>-1</sup> (main text) and loss to dark (that is, not repumped) vibrational states,  $R_{\rm vib}$  =  $\Gamma_{\rm scatt}/N_{\rm phot}$ , where  $N_{\rm phot}$  = 1.6 × 10<sup>4</sup> is the vibrational

repumping-limited average number of photons scattered per molecule. The total loss rate  $R_{\rm loss} = R_{ij} + R_{\rm vib} + R_{\rm vac}$  is calculated as a function of tweezer wavelength using the fitted Rabi frequencies and centre wavelengths from the a.c. Stark shift data.

Extended Data Fig. 1 shows the number of photons scattered per molecule in the experiment (measured as described above) as a function of tweezer wavelength. We also plot the calculated photon number determined from the loss rate calculations,  $N_{\rm im} = \Gamma_{\rm scatt}/R_{\rm loss}$  (blue, solid curve). Here we have used the known loss rates  $R_{\text{vac}}$  and  $R_{\text{vib}}$  as well as the measured Rabi frequencies and wavelengths for tweezerinduced excited-state loss. The only unknown parameter is  $\Gamma_{ij}$ , the loss rate from the high-lying states to which the tweezer couples, which was assumed to be constant for all excited states and varied to match the measured photon number data. We find reasonable agreement with the experimental data using an excited-state loss rate  $\Gamma_i \approx 2\pi \times 75$  MHz, corresponding to a lifetime of  $\Gamma_i^{-1} \approx 2.1$  ns. The remaining disagreement, particularly in the 784-786 nm range, may be attributed to the effect of other excited state resonances that were not considered in the a.c. Stark shift data. For example, there is a known resonance from  $\widetilde{A}^2\Pi_{1/2}(000) \leftrightarrow \widetilde{D}^2\Sigma^+(010)$  at 793.6 nm (ref. 53). Including this state, assuming the same Rabi frequency measured for the  $\widetilde{A}^2\Pi_{1/2}(000) \leftrightarrow \widetilde{D}^2\Sigma^+(100)$  transition at 777.9 nm, results in better agreement with the experimental data (black, dashed curve).

The inferred approximately 2 ns lifetime of the high-lying electronic states is an order of magnitude shorter than the radiative lifetime of the lower-lying  $\widetilde{A}^2\Pi$  and  $\widetilde{B}^2\Sigma^+$  states in CaOH. This could indicate non-radiative loss mechanisms for these states, as hypothesized for similar states in tweezer-trapped diatomic molecules  $^{55,64}$ .

#### **Imaging fidelity**

The imaging fidelity is defined as the probability of correctly identifying whether a trap is initially empty (0 molecules) or loaded (1 molecule in the collisional blockade regime). Specifically, it may be defined in terms of the error rates  $\epsilon_{01}$  (incorrectly identifying an empty trap as loaded; 'false positive') and  $\epsilon_{10}$  (incorrectly identifying a loaded trap as empty; 'false negative') as follows:  $f(p) = 1 - p\epsilon_{10} - (1 - p)\epsilon_{01}$ , where p is the tweezer loading probability<sup>55</sup>.

The error rates depend on the threshold number of counts,  $\theta$ , used to distinguish loaded and empty traps. The false positive rate,  $\epsilon_{01}(\theta)$ , is determined by analysing histogram data for empty traps, which can be collected by taking images of tweezers guaranteed to be empty by, for example, turning off the molecule source. The histogram data,  $h_0(n)$ , is a function of the number of image counts n, and is normalized so that  $\sum_n h_0(n) = 1$ . Moreover, we define a cumulative probability distribution for the histogram data,  $g_0(\theta) = \sum_{n=0}^{\theta} h_0(n)$ . Following these definitions, the false positive rate  $\epsilon_{01}(\theta)$  is simply the probability of collecting greater than  $\theta$  counts from an image of an empty trap, namely,  $\epsilon_{01}(\theta) = 1 - g_0(\theta)$ .

To determine the false negative rate  $\epsilon_{10}(\theta)$ , we must infer the histogram of image counts collected from loaded traps,  $h_1(n)$ . Because the loading rate is much less than 1 in the experiment, this requires subtracting out the effect of empty traps from  $h_{\rm exp}(n)$ , the measured histogram data. This is done by scaling the empty trap histogram data  $h_0(n)$  by a factor of (1-p) (the probability of a trap being empty), subtracting this from the experimental data to remove the background contribution, and renormalizing the result:  $h_1(n) = [h_{\rm exp}(n) - (1-p)h_0(n)]p^{-1}$ . We discuss how p is determined below. The cumulative probability distribution for loaded traps is defined as  $g_1(\theta) = \sum_{n=0}^{\theta} h_1(n)$ , and the false negative error rate is the probability of collecting fewer than  $\theta$  counts from a loaded tweezer,  $\epsilon_{10}(\theta) = g_1(\theta)$ .

Determining p, the tweezer loading probability, is equivalent to finding the scale factor to apply to  $h_0(n)$  so that the empty trap background is appropriately subtracted from  $h_{\rm exp}(n)$  in the procedure above. To perform this background subtraction, we take advantage of the tall (approximately 80% of the counts in  $h_0(n)$ ), zero-photoelectron peak

generated by the EMCCD camera, which is approximately Gaussian in shape with a standard deviation of  $\sigma_r \approx 4$  digital counts (given by the camera readout noise), and is centred at zero photoelectron counts (far left side of the histogram). We isolate this peak in both the signal and background histograms, then apply a scale factor of (1-p) to the empty histogram data and calculate the sum of squared differences between the two,  $S(p) = \sum_{n=n_i}^{n_f} [h_{\rm exp}(n) - (1-p)h_0(n)]^2$ , where  $n_i$  and  $n_f$  are the lower and upper edges of the peak. The value of p that minimizes S(p) is the inferred loading probability for the experimental data and is used to determine  $h_1(n)$  via the procedure defined above.

A necessary assumption of the background subtraction procedure is that the zero-photoelectron peak in the experimental data arises purely from empty traps, meaning that we can rescale the background histogram to match the height of this peak and assume that the result accurately reflects the distribution of empty trap counts in the experimental data. This approximation is justified by the fact that the average number of counts arising from loaded traps,  $\overline{n}$ , is hundreds of counts above the zero-photon peak  $(\overline{n} \gg \sigma_r)$ , so that any residual tail at low count numbers is negligible compared to the contribution from empty traps. By benchmarking the background subtraction procedure against simulated histogram data with varying fractions of the zero-photon counts arising from loaded traps, we conservatively estimate that this approximation could bias the calculated fidelity up to 2% above the true value for our experimental parameters. Systematic errors due to differing scattered light and camera noise environments between the experimental datasets  $h_0(n)$  and  $h_{exp}(n)$  contribute at the 1% level.

Extended Data Fig. 2 illustrates the fidelity results for 7 ms tweezer images, chosen to be short enough for reasonably high molecule survival after imaging. Extended Data Fig. 2a shows the signal and background histograms  $(h_{\text{exp}}(n))$  and  $h_0(n)$ , respectively) from which the error probabilities  $\epsilon_{01}(\theta)$  and  $\epsilon_{10}(\theta)$  are inferred using the procedure described above. These error rates are plotted as a function of the threshold value  $\theta$  in Extended Data Fig. 2b. Higher choices of threshold reduce the probability of misidentifying empty traps as loaded ( $\epsilon_{01}$ , blue curve), at the expense of increasing the likelihood of misidentifying loaded traps as empty ( $\epsilon_{10}$ , red curve). Extended Data Fig. 2c shows the imaging fidelity,  $f(p,\theta) = 1 - p\epsilon_{10}(\theta) - (1-p)\epsilon_{01}(\theta)$ , as a function of detection threshold for various loading probabilities. Each curve exhibits a peak corresponding to the optimal tradeoff between the two misidentification error sources. For higher loading probabilities, a lower threshold optimizes the fidelity, since reducing the likelihood of misidentifying loaded traps as empty becomes more important at higher loading rates. For all loading rates. fidelities  $f \ge 0.94$  are possible for an appropriate choice of threshold.

Combining the systematic error sources above with a statistical error of approximately 1.5% obtained using a bootstrapping procedure, we determine that the imaging fidelity is  $f = 0.94^{+0.02}_{-0.03}$  for the 7 ms tweezer images at an optimal threshold of  $\theta \approx 700$  and a measured loading rate of p = 0.34.

#### Single-molecule loading

We quantify the fraction of tweezers that contain more than one molecule by comparing the average brightness of loaded tweezers for the two histograms in Fig. 1b, which differ in loading rate by a factor of 2.4. Specifically, we isolate the loaded portion of the histogram using a threshold value  $\theta$ , and calculate the average number of camera counts above the threshold for the two histograms. The brightness ratio, along with the known loading probabilities for the two histograms, can be used to constrain the number of doubly occupied tweezers represented in the histogram data.

We model the number of molecules n loaded in the tweezers using a Poisson distribution,  $P(n; \lambda)$ , where  $\lambda$  is the average loading rate. Because the loading fraction is significantly less than 50%, we assume that  $\lambda < 1$ . We therefore approximate  $P(n = 3; \lambda) \approx \lambda^3/6 \approx 0$  and only consider the case where zero, one, or two molecules are loaded. Additionally, to quantify the efficiency of the collisional blockade we assign a

probability  $\beta$  that two initially loaded molecules survive to the start of the imaging, that is, that they fail to undergo a light-assisted collision. Under these assumptions, the measured loading probability is

$$p = P(n=1;\lambda) + P(n=2;\lambda)\beta$$
 (3)

and the average image brightness, per loaded molecule, is

$$\overline{B} = a[P(n=1;\lambda) + 2\zeta P(n=2;\lambda)\beta]/p \tag{4}$$

where a is the brightness of a single molecule. The threshold-dependent scale factor,  $\zeta \le 1$ , captures an effect where doubly occupied traps appear, on average, less than twice as bright as singly occupied traps due to the finite single-molecule imaging lifetime, since molecules that are lost early in the imaging are thresholded out in the analysis. For purposes of this analysis we neglect light-assisted collisions that occur during the imaging pulse. For a threshold of  $\theta = 1,100$ , we calculate  $\zeta \approx 0.89$  using the known single-molecule imaging lifetime and imaging efficiency.

The loading fractions are  $p_1$  = 0.314(15) and  $p_2$  = 0.134(9), where the subscripts 1 and 2 correspond to the orange and purple histograms in Fig. 1b, respectively. The thresholded average brightness values for the two histograms are  $\overline{B}_1 = \sum_{n=0}^{\infty} nh_1(n)/\sum_{n=0}^{\infty} h_1(n) - \mathcal{C}$  and  $\overline{B}_2 = \sum_{n=0}^{\infty} nh_2(n)/\sum_{n=0}^{\infty} h_2(n) - \mathcal{C}$ , where  $h_i(n)$  is the experimental histogram data, n is the number of camera counts and  $\mathcal{C}$  = 501 is the number of camera counts corresponding to zero detected photons. Combining these definitions, we write down a system of equations that can be solved for the loading rates  $\lambda_1$  and  $\lambda_2$  along with the two-molecule survival probability  $\beta$ :

$$p_{1} = P(1; \lambda_{1}) + P(2; \lambda_{1})\beta$$

$$p_{2} = P(1; \lambda_{2}) + P(2; \lambda_{2})\beta$$

$$\frac{\overline{B}_{1}}{\overline{B}_{2}} = \frac{P(1; \lambda_{1}) + 2\zeta P(2; \lambda_{1})\beta}{P(1; \lambda_{2}) + 2\zeta P(2; \lambda_{2})\beta} \times \frac{p_{2}}{p_{1}}$$
(5)

For a threshold of  $\theta$  = 1,100, near the minimum between the two peaks in the histogram data, we find  $\lambda_1$  = 0.39(19),  $\lambda_2$  = 0.13(6) and  $\beta$  = 0.28(29), where the error bars are determined using bootstrapping. The fraction of loaded traps that contain more than one molecule is therefore  $P(2;\lambda_1)\beta/p_1$  = 0.05(5) for the  $p_1$  = 0.31 histogram (orange data) and  $P(2;\lambda_2)\beta/p_2$  = 0.02(2) for the  $p_2$  = 0.13 histogram (purple data).

### **Data availability**

The data that support the findings of this study are available from the corresponding author on reasonable request. Source data are provided with this paper.

- Anderegg, L. Ultracold Molecules in Optical Arrays: From Laser Cooling to Molecular Collisions. PhD thesis. Harvard Univ. (2019).
- Truppe, S. et al. An intense, cold, velocity-controlled molecular beam by frequencychirped laser slowing. New J. Phys. 19, 022001 (2017).
- Zhang, C. et al. Accurate prediction and measurement of vibronic branching ratios for laser cooling linear polyatomic molecules. J. Chem. Phys. 155, 091101 (2021).
- Yu, Y. et al. Coherent optical creation of a single molecule. Phys. Rev. X 11, 031061 (2021).

Acknowledgements We thank L. Cheng for providing dynamic polarizability calculations. This work was supported by the AFOSR, NSF, and ARO. Support is also acknowledged from the U.S. Department of Energy, Office of Science, National Quantum Information Science Research Centers, Quantum Systems Accelerator. P.R. acknowledges support from the NSF GRFP, and G.K.L. and L.A. acknowledge support from the HQI.

**Author contributions** N.B.V., P.R., C.H., G.K.L. and L.A. performed the experiment and analysed the data. J.M.D. directed the study. All authors discussed the results and contributed to the manuscript.

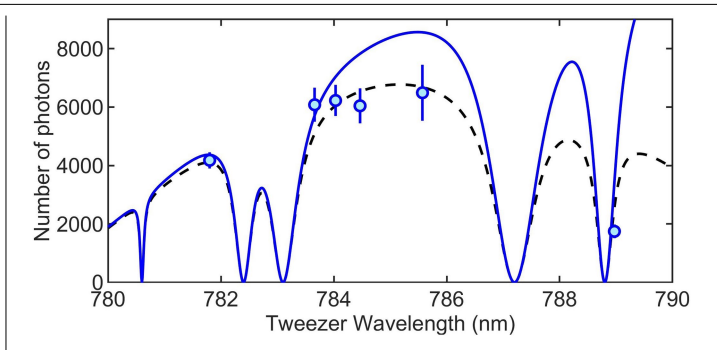
Competing interests The authors declare no competing interests.

#### Additional information

Correspondence and requests for materials should be addressed to Nathaniel B. Vilas.

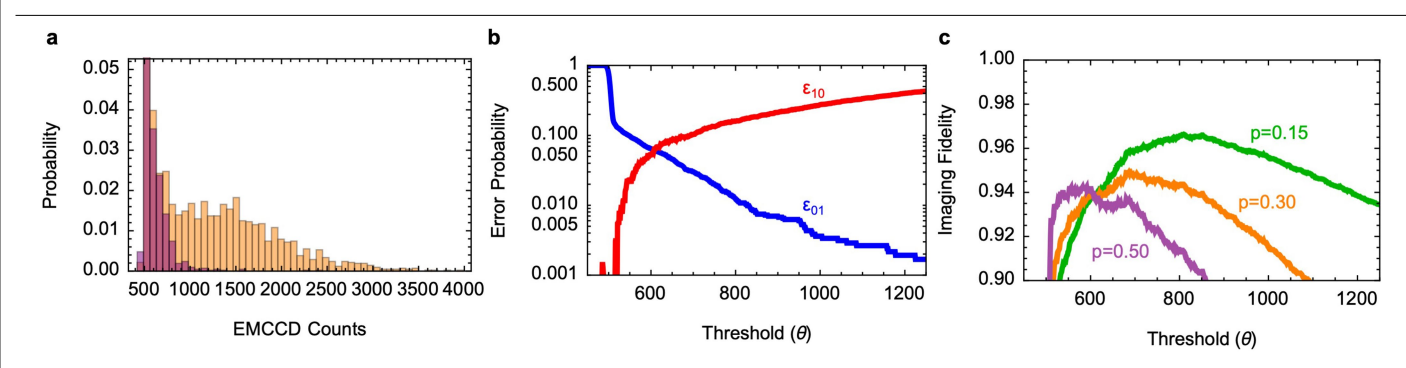
Peer review information Nature thanks the anonymous reviewers for their contribution to the peer review of this work.

Reprints and permissions information is available at http://www.nature.com/reprints.



# $Extended\,Data\,Fig.\,1|\,Imaging\,photon\,budget\,vs.\,tweezer\,wavelength.$

Calculated (curves) and measured (points) number of imaging photons that can be scattered during molecule imaging in the tweezer array, as a function of the trapping wavelength. Calculations include the effect of vacuum loss, loss to vibrational dark states, and trap-wavelength-dependent excitation to lossy excited electronic levels. The solid blue curve accounts for excitation only to those states observed using AC Stark shift data, while the black, dashed curve additionally includes  $\overline{A}^2\Pi_{1/2}(000) \leftrightarrow \overline{D}^2\Sigma^+(010)$  excitation predicted at 793.6 nm.



**Extended Data Fig. 2** | **Determination of tweezer imaging fidelities. a**, Signal (orange) and background (purple) histogram data,  $h_{\rm exp}(n)$  and  $h_0(n)$ , for 7 ms tweezer images. The average tweezer loading probability in the signal histogram is p=0.34. **b**, Misidentification error rates  $\epsilon_{\rm Ol}(\theta)$  and  $\epsilon_{\rm IO}(\theta)$  for 7 ms

tweezer images, inferred from the experimental data as described in the text.  $\mathbf{c}$ , Imaging fidelities f(p) for several average tweezer loading probabilities p, as described in the text.